Toroidal Inductor Design in Multilevel DC-DC Electric Vehicle Battery Charger Including High-Frequency Effects

David Elizondo, Ernesto L. Barrios, and Pablo Sanchis
Institute of Smart Cities (ISC), Dept. of Electrical, Electronic and Communications Engineering
Public University of Navarre (UPNA), Campus Arrosadia, 31006
Pamplona, Spain
david.elizondo@unavarra.es

Abstract—**Inductor filters, such as the ones implemented in DC-DC buck-boost converters for electric vehicle chargers, have a major impact on the converter weight, volume and cost. Thus, their design is key in order to obtain an optimal design of the whole converter. This paper proposes a design methodology for powder core toroidal inductors, which is based on a holistic approach of the design of the inductor, where losses due to high-frequency effects are computed by means of specific loss model for toroidal windings, and saturation, geometrical and thermal constraints are considered. The convenience of the design tool is shown through an analysis over a wide variation of parameters, including converter topology, parallelization, switching frequency and inductance. The analysis demonstrates the relevance of high-frequency effects on the inductor design, so certain misconceptions can be avoided, such as that the inductor volume monotonically decreases when the inductance value is decreased or that paralleling inductors always results in more compact designs. A design example is presented for a 15-kW, three-level electric vehicle battery charger. The algorithm is used to obtain an optimal design of the converter, including the inductors and SiC MOSFET devices. Finally, an easy method to obtain a commercial inductor design from the theoretical one provided by the algorithm is presented.**

Keywords— toroidal inductor, high-frequency effects, winding loss, optimization algorithm, multilevel dc-dc converter, electric vehicle.

I. INTRODUCTION

DC-DC buck-boost converters are implemented in multiple applications, e.g., PV systems [1], [2], grid-connected systems with integrated energy storage [3], [4], fuel cell electric vehicles [5] and battery power systems for electric vehicles (EV) [6], [7]. Powder core toroidal inductors are often selected for these power applications [5], [6] due to their low price, high saturation flux density and soft-saturation characteristic [8]. Inductors in DC-DC buck-boost converters operate under a high-frequency rectangular voltage, thus under a non-sinusoidal excitation. As a consequence, the estimation of the power losses must consider that there is a DC current component in the coil along with a high-frequency triangular current ripple. The former is responsible of the DC winding loss and the latter is accountable for the AC winding loss, which is greater if the frequency of the ripple increases for a given coil [9]. Additionally, there are losses in the magnetic core, which are also dependent on the frequency of the excitation and on the shape of this excitation too, which is rectangular in buck-boost converters. As a result, the total power losses in the inductor are the sum of the DC winding loss, the AC winding loss and the core loss, the last two due to high frequency (HF) effects. The HF effects can play a key role in the inductor losses [10], hence conditioning the thermal design. If the power losses of the inductor are underestimated during the design process, the resultant component will overheat. Therefore, it will be unable to work under the required operating conditions. On the other hand, if the design overestimates the losses, the inductor will be too bulky.

The inductors of the output filter have a major impact on the weight, volume and cost of the buck-boost converters. Hence, a proper design process which includes HF effects in the inductor is needed in order to achieve an optimal design of the entire converter. Nevertheless, several design methods for inductors in switching converters lack the inclusion of AC winding loss [11], [12]. Other papers, which do include the HF effects on the winding [13], [14], use models which are not specific for toroidal windings, thus leading to significant overestimation of the winding loss [15]. The proposed design method calculates the AC winding loss in round-wire toroidal inductors through a model which has demonstrated to be accurate and easy to implement into design algorithms [15]. Moreover, the core loss estimation considers a non-sinusoidal excitation case, since the magnetizing voltage is a rectangular waveform dependent on the duty cycle. As a result, the optimization algorithm follows a holistic approach, including HF effects, roll-off influence on the inductance value, and saturation, geometrical and thermal constraints.

The algorithm is applied to the design of toroidal inductors in the output filter of a 15-kW buck-boost converter for EV battery charging. The usefulness of the algorithm regarding trend analysis and optimal design identification is demonstrated by means of sweeps in various key parameters, such as converter topology (two-level and three-level), number of parallel converters, N_B, switching frequency, f_{sw}, and initial inductance value, L_0. The design algorithm is based on a full parameterization of the inductor, which is introduced first. Then, the power losses and thermal models are presented and expressed including the parameterization. The design constraints are parameterized too. The result is an optimization tool which considers only three design variables: core width, wire radius and core magnetic permeability. Results for optimal volume of the inductor are obtained considering a wide range of f_{sw} and L_0. A thorough analysis of the results is performed and optimal inductor designs for each topology are identified. A design example for a 15-kW, three-level EV charger is also presented. The optimal design is obtained, including the SiC MOSFET semiconductor system and the inductors. Finally, an easy method to adapt the analytical inductor solution provided by the algorithm to a commercial design is introduced.

II. DESCRIPTION OF THE APPLICATION

The proposed optimization algorithm is implemented for the design of powder-core toroidal inductors in a 15-kW DC-DC electric vehicle battery charger. The requirements of the application are summarized in the operating area depicted in Fig. 1 and the characteristics presented in Table I. For this application, two topologies are considered. The simplest one is the two-level (2L) buck-boost, depicted in Fig. 2 (a). The next step in complexity is the three-level (3L) topology, which is shown in Fig. 2 (b). Moreover, one ($N_B = 1$) and two converters in parallel ($N_B = 2$) are considered in the design.

TABLE I.   REQUIREMENTS OF THE CONVERTER

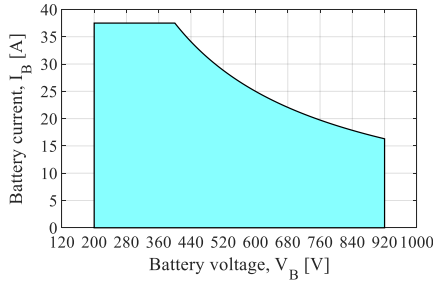| Symbol	Parameters	
	Description	*Value*
P_{max}	Rated power [kW]	15
$I_{dc,max}$	Rated DC current [A]	37.5
V_i	Input voltage [V]	1000
$V_{B,min}$	Minimum battery voltage [V]	200
$V_{B,max}$	Maximum battery voltage [V]	920
$f_{sw,min}$	Minimum switching frequency [kHz]	20
T_a	Rated ambient temperature [ºC]	55
T_{max}	Max. hot spot temperature allowed [ºC]	130

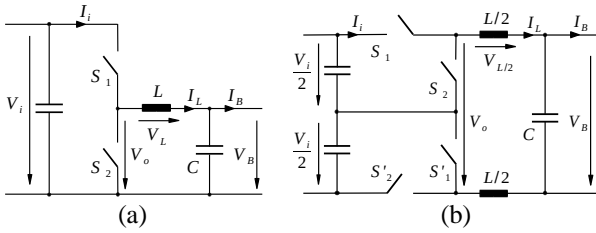Fig. 1.   Operating area of the converter.

Fig. 2.   Considered topologies of buck-boost: (a) 2L, (b) 3L.

A. Two-Level (2L) Buck-Boost Converter

A 2L buck-boost converter comprises of a single switching cell. Thus, it provides only two levels of voltage at the output, V_o, which are 0 and V_i. In the 2L buck-boost converter, the voltage applied to the battery, V_B, is defined as $V_B = V_i d$, being d the duty cycle. The instantaneous voltage applied to the inductor is $V_L = V_o - V_B$, which is $V_i(1 - d)$ when S_1 is on, and $-V_i d$ when S_2 is on. As a consequence, the peak-to-peak value of the current ripple in the inductor can be defined by means of the duty cycle as:

$$I_{ac,pp,2L} = \frac{V_i d(1 - d)}{f_{sw} L},\qquad(1)$$

where f_{sw} is the switching frequency and L is the effective inductance value at maximum peak current. The main

waveforms in a 2L converter are depicted in Fig. 3 (a) for rated power, $L = 300 \,\mu H$, $f_{sw} = 36 \,kHz$, and a battery voltage of 400 V. As can be deduced from (1), the maximum current ripple and thus, the maximum peak value of the induction, B_p, takes place at $d = 0.5$. Considering the operating area of the converter, this working point is $V_B = 500 \,V$, $I_B = 30 \,A$ at rated power. Nevertheless, the closest point with maximum DC current is $P = 15 \,kW$, $V_B = 400 \,V$, $I_B = 37.5 \,A$. Therefore, in the inductor design in 2L converters, it is enough to consider the range between $d = 0.4$ and $d = 0.5$, which includes the inductor maximum losses point.

B. Three-Level (3L) Buck-Boost Converter

The 3L topology is built from two switching cells. This configuration allows three voltage levels at the output, which are 0, $V_i/2$ and V_i. The battery voltage can be defined as in the 2L buck-boost: $V_B = V_i d$. As a result, the peak-to-peak value of the current ripple is:

$$I_{ac,pp,3L} = \frac{V_i d(1 - 2d)}{2 f_{sw} L},\qquad(2)$$

which appears at twice the switching frequency. In this case, the maximum peak value takes place at $d = 0.25$ and $d = 0.75$. The main waveforms in a 3L buck-boost are depicted in Fig. 3 (b) for rated power, $L = 300 \,\mu H$, $f_{sw} = 36 \,kHz$, and a battery voltage of 400 V. At rated power, maximum DC and AC current intensities meet at the same operating point: $V_B = 250 \,V$ and $I_B = 37.5 \,A$. Hence, the design of the inductor in the 3L buck-boost converter needs to consider only one point, which is $d = 0.25$ at rated power.
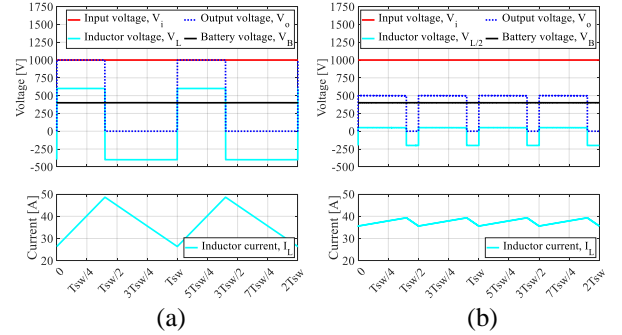

Fig. 3.   Main waveforms in buck-boost: (a) 2L, (b) 3L.

III. INDUCTOR MODELING AND OPTIMIZATION ALGORITHM

The design of a high-frequency power inductor is a complex task, since there are many parameters involved. Moreover, three loss mechanisms interact in the coil design, namely DC winding loss ($P_{\omega,dc}$), AC winding loss ($P_{\omega,ac}$) and core loss (P_c), the last two caused by HF effects. The proposed optimization algorithm is based on a geometrical parameterization of the inductor, so all the characteristic dimensions can be defined by means of a set of parameters, the core width, a, and the wire radius, R. Adding the initial relative permeability of the core, μ_r, as a variable, the optimization algorithm reduces the problem to three optimization variables: a, R and μ_r. All the rest of variables of the optimization problem can be expressed as functions of these three variables. Additionally, the design tool incorporates models of the three mentioned loss mechanisms, hence providing an accurate estimation of the power losses of the inductor.

A. Geometrical Parameterization of the Inductor

The toroidal inductor can be parameterized as in Table II, where the characteristic dimensions are defined through the geometrical variables a and R, and the parameters c_1, c_2 and K_{dt}. The main characteristic dimensions are also depicted in Fig. 4 (a) and (b). Coefficients c_1 and c_2 are related to the radius of the core window and the height of the core, respectively. The winding factor, WF, can be expressed through factor K_{dt}, which can be defined as $K_{dt} = \left(1 - \sqrt{1 - WF}\right)$. As can be seen in Table II, K_{dt} modifies V_e and S_e. The equivalent volume, V_e, is the total volume (core and winding) occupied by the inductor and the equivalent surface, S_e, is the effective convection surface. Typically, a maximum winding factor of 40% is assumed for toroidal coils, which is the value considered in the optimization algorithm. It is to be noted that factor A_{FR} is specific of toroidal inductors and plays a key role in the power loss due to the proximity effect in the winding. It is defined as the ratio between the radius of the toroidal core window, $c_1 a$, and the radius of the wire, R [15].

TABLE II.   CHARACTERISTIC DIMENSIONS OF TOROIDAL INDUCTORS

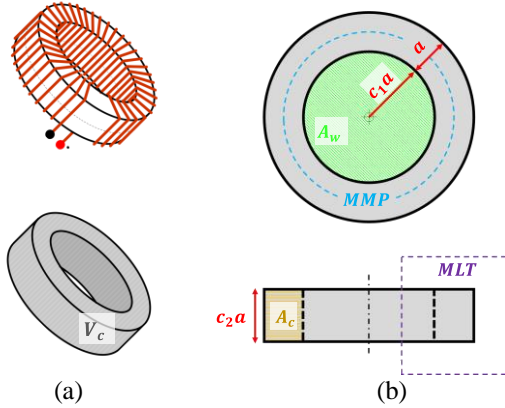| Description	Parameters	
	Symbol and expression	Compact form
Diameter ratio	$A_{FR} = ac_1/R$	$a/R \cdot a_{FR}$
Mean length of turn	$MLT = a(2c_1 K_{dt} + c2 + 1)2$	$a \cdot mlt$
Core cross section	$A_c = a^2 c_2$	$a^2 \cdot a_c$
Core window area	$A_w = a^2 \pi c_1^2$	$a^2 \cdot a_w$
Mean magnetic path	$MMP = a(2c_1 + 1)\pi$	$a \cdot mmp$
Core volume	$V_c = a^3(2c_1 + 1)\pi c_2$	$a^3 \cdot v_c$
Equivalent volume	$V_e = a^3(c_1(2 + K_{dt}) + 2)^2 (c1K_{dt} + 2c_2)\,\pi/8$	$a^3 \cdot v_e$
Equivalent surface	$S_e =$ $= a^2(6c_1^2 K_{dt} + c_1(3K_{dt} + 4c_2 + 4) + 2c_2 + 2)\pi$	$a^2 \cdot s_e$

Fig. 4. Main geometrical parameters of a toroidal inductor: (a) 3D view, (b) 2D views.

B. Power Loss Calculation

Power loss calculation comprises of DC winding loss, $P_{\omega,dc}$, AC winding loss, $P_{\omega,ac}$, and core loss, P_c. The DC winding loss can be defined as follows:

$$P_{\omega,dc} = R_{dc}I_{dc}^2 = N\frac{MLT}{\sigma\pi R^2}I_{dc}^2,   (3)$$

where N is the number of turns of the coil, σ is the electrical conductivity of the wire and I_{dc} is the inductor DC current. The number of turns can be expressed by means of the inductance formula:

$$L_0 = \mu_0\mu_r N^2 A_c/MMP \Rightarrow N = \sqrt{\frac{L_0 MMP}{A_c\mu_0\mu_r}},   (4)$$

where L_0 is the initial inductance value under zero magnetizing force, that is, with null current intensity. Then, the expressions in Table II for MLT, MMP and A_c can be introduced into (3), which results in:

$$P_{\omega,dc} = \sqrt{\frac{a}{\mu_r}\frac{1}{R^2}}\sqrt{\frac{L_0 mmp}{a_c\mu_0}}\frac{mlt}{\sigma\pi}I_{dc}^2.   (5)$$

In the case of toroidal windings, applying classical models to calculate the HF winding loss, such as Dowell's model [9], can lead to a significant overestimation. Therefore, the optimization algorithm implements the AC winding loss model in [15], which properly considers that the magnetic field in toroidal inductors is two-dimensional and different for each layer and winding section. The AC winding loss can be defined by means of the resistance factor, $F_{R,h}$, as follows:

$$P_{\omega,ac} = R_{dc}\sum_{h=1}^{\infty}F_{R,h}I_{ac,h}^2,   (6)$$

where h is the order of the harmonic and $I_{ac,h}$ is the rms current intensity of the hth harmonic. For toroidal inductors, the following expression for $F_{R,h}$ can be used [15]:

$$F_{R,h} = \frac{1}{2}\Big[\Delta_h^i\psi_{1,h}\big(\Delta_h^i\big) + \Delta_h^o\psi_{1,h}\big(\Delta_h^o\big) + \frac{\phi}{b} + \frac{\phi}{b}\Big(\Delta_h^i\psi_{2,h}\big(\Delta_h^i\big) + \Delta_h^o\psi_{2,h}\big(\Delta_h^o\big)\Big)\Big],   (7)$$

where Δ_h^i and Δ_h^o are the penetration ratio particularized for the packing factor of the inner section and the outer section of the toroidal winding, respectively. Then, $\psi_{1,h}$ is a function related to the skin effect and $\psi_{2,h}$ is a function related to the proximity effect [16]. Factor ϕ/b is specific for proximity losses in toroidal windings and only dependent on A_{FR} and the number of layers, m, which can be parameterized as follows:

$$m = \frac{A_{FR}}{2} - \sqrt{\frac{A_{FR}^2}{4} - \frac{N}{\pi}} =$$
$$= a\left(\frac{a_{FR}}{2} - \sqrt{\frac{a_{FR}^2}{4} - \frac{\sqrt{L_0 mmp}}{\pi\sqrt{\mu_0 a_c}a^{3/2}\mu_r^{1/2}}}\right)   (8)$$

As can be seen, the resistance factor, and thus $P_{\omega,ac}$, can be completely parameterized and expressed as a function of the variables a, R and μ_r.

Finally, the core loss can be calculated by means of the Steinmetz equation or its variants. For non-sinusoidal magnetization, the modified Steinmetz equation (MSE) can be used [17]:

$$P_c = 1000k_{mag}C_m f_1^x B_p^y V_c(c_{T2}T^2 - c_{T1}T + c_{T0}),   (9)$$

because it provides a satisfactory trade-off between accuracy and simplicity to be implemented in a design algorithm [18]. In the MSE, k_{mag} is defined as the core loss waveform coefficient, which relates the loss under the actual magnetic induction to the loss under a sinusoidal waveform, C_m, x and

y are core loss coefficients of the magnetic material, f_1 is the frequency of the magnetizing voltage, B_p is the peak value of the induction, and c_{T2}, c_{T1}, c_{T0} are coefficients that express the dependence of the magnetic material loss with the temperature, T. Core loss in powder core materials is not influenced by the temperature ($c_{T2}, c_{T1} = 0$ and $c_{T0} = 1$). Thus, the temperature-dependent factor can be removed from (9) in this case. Regarding that the inductor is under a rectangular voltage waveform excitation case with a duty cycle d, k_{mag} can be expressed as [19]:

$$k_{mag} = \left(\frac{4}{\pi^2 d}\right)^{x-1}, \qquad (10)$$

and B_p can be defined as follows for 2L and 3L topologies by means of the Faraday's law:

$$B_{p,2L} = V_i(1-d)d/(2f_1 N A_c),$$
$$B_{p,3L} = V_i(1-2d)d/(2f_1 N A_c). \qquad (11)$$

It is important to note that f_1 is the frequency of the magnetizing voltage, which is f_{sw} in 2L converters and $2f_{sw}$ in 3L converters. If the parameterized expressions of N and A_c are introduced into (11), the induction peak value becomes:

$$B_{p,2L} = V_i(1-d)d\sqrt{\mu_0 \mu_r}/(2f_1 a^{3/2}\sqrt{a_c L_0 mmp}),$$
$$B_{p,3L} = V_i(1-2d)d\sqrt{\mu_0 \mu_r}/(2f_1 a^{3/2}\sqrt{a_c L_0 mmp}). \qquad (12)$$

Introducing the parameterized expressions of B_p in (12) and V_c into (9), the core loss expression becomes:

$$P_c = 1000 k_{mag} C_m f_1^{x-y} \frac{V_m^y \mu_0^{y/2} v_c a^{3-3y/2} \mu_r^{y/2}}{(a_c L_0 mmp)^{y/2}}, \qquad (13)$$

where $V_m = V_i(1-d)d/2$ in 2L topologies and $V_m = V_i(1-2d)d/2$ in 3L topologies. It must be noted that core loss coefficients C_m, x and y can be dependent on the initial permeability, μ_r. Therefore, C_m, x and y can be adjusted as functions of μ_r from the datasheet of the magnetic material.

C. Relative permeability roll-off

Powder cores are known for having a soft-saturation characteristic, as represented in Fig. 5 (a) for the magnetic material Sendust and four different values of relative permeability, μ_r. Under zero magnetizing force, that is zero current intensity, the relative permeability of the core is its initial value, μ_r, which is a design variable in the proposed methodology. Hence, the inductance value is L_0, as defined in (4). Then, the effective inductance at maximum peak current is L. Thus, it is the inductance value considered when calculating the current ripple in the inductor design process. The maximum design roll-off, which is the percentage of reduction in relative permeability that it is allowed in the core at maximum magnetizing force condition, is subject to the designer's decision. In this paper, a maximum roll-off of 50% is allowed. As a consequence, since the roll-off relates the inductance values L_0 and L by means of the following expression:

$$L = L_0(1 - \text{roll-off}), \qquad (14)$$

the effective inductance becomes $L = L_0/2$. In other words, if a certain L value is required in order to meet a current ripple requirement, the objective inductance value of the design will be $L_0 = 2L$ if a 50% roll-off is allowed.
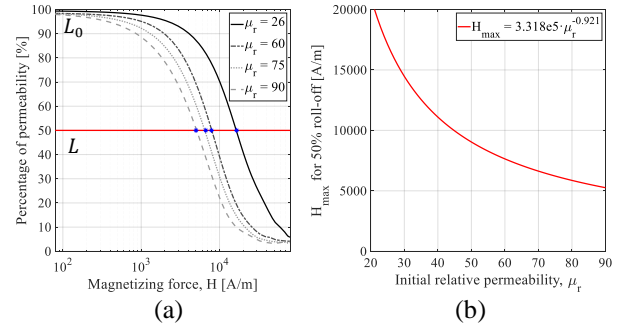

Fig. 5. Sendust magnetic core material: (a) permeability vs. magnetizing force, (b) maximum magnetizing force for 50% roll-off.

D. Thermal Model

The designed inductor is unboxed and passively cooled. The thermal resistance of the inductor is modelled using an empirical formula for inductors in still air [20]:

$$R_{th} = \frac{1}{(10 s_e a^2)^{0.833} \cdot P_{ind}^{0.167}}, \qquad (15)$$

where $P_{ind} = P_\omega + P_c$, which are the power losses of the inductor, and s_e is the effective surface to convective cooling of the component, as defined in Table II.

E. Optimization Problem

The proposed optimization algorithm can consider two possible design criteria: the efficiency criterion, i.e. minimize total losses, P_{ind}, and the volume criterion, that is minimize the equivalent volume, V_e. In this paper, the volume criterion is selected and the optimization problem becomes:

$$\min \quad V_e, \qquad (16)$$

subject to three design constraints: core window, saturation and thermal constraints. The core window constraint is expressed as:

$$m - \left(1 - \sqrt{1 - WF}\right) \cdot A_{FR}/2 \le 0, \qquad (17)$$

and it ensures that the number of layers, m, fit in the core window. The maximum winding factor, WF, limits the maximum number of layers and thus, maximum number of turns. According to [20], a maximum WF of 40% can be assumed in toroidal inductors due to limitations of space and packing factor of the winding during manufacturing.

Then, the saturation constraint guarantees that the magnetic field intensity of the coil does not surpass the maximum magnetic field intensity, H_{max}, for a certain roll-off limit in the permeability of the core, which is a design criterion, as previously mentioned. In this paper, a maximum roll-off of 50% in the permeability is defined. Taking a set of (μ_r, H) points at 50% roll-off from the magnetic material datasheet, as shown in Fig. 5 (a), H_{max} can be fitted as a function of the initial permeability:

$$H_{max} = p \cdot \mu_r^q, \qquad (18)$$

where p and q are coefficients, as exemplified in Fig. 5 (b) for the magnetic material Sendust [21]. The saturation constraint is defined for the maximum peak value of the current, which is $I_{dc} + I_{ac,p}$. As a result, the saturation constraint can be expressed as:

$$\left(I_{dc} + I_{ac,p}\right)N/MMP - H_{max} \le 0. \qquad (19)$$

The peak value of the current ripple, $I_{ac,p}$, can be defined from (1), (2) and (14) as follows:

$$I_{ac,p} = V_m/(f_1 L_0 (1 - rolloff)), \qquad (20)$$

being $V_m = V_i(1-d)d/2$ and $f_1 = f_{sw}$ in 2L topologies, and $V_m = V_i(1-2d)d/2$ and $f_1 = 2f_{sw}$ in 3L topologies.

Introducing the parameterization of N and MMP, and the expression of H_{max} and $I_{ac,p}$, into (19), the saturation constraint becomes:

$$\left(I_{dc} + \frac{V_m}{f_1 L_0 (1-rolloff)}\right)\sqrt{\frac{L_0}{\mu_0 a_c mmp}}\sqrt{\frac{1}{\mu_r a^3}} - p\mu_r^q \le 0. \qquad (21)$$

Finally, the thermal constraint can be expressed as follows:

$$T - T_{max} \le 0 \Rightarrow P_{ind}R_{th} + T_a - T_{max} \le 0, \qquad (22)$$

being T_a the ambient temperature and T_{max} the maximum allowed temperature of the inductor, which is 130 ºC.

IV. RESULTS AND ANALYSIS

The proposed algorithm is used to design toroidal inductors for the output filter of a 15-kW buck-boost EV battery charger. The basic input parameters are included in Table I. Additionally, several parameters and boundaries are to be defined in the algorithm, such as the lower and upper boundaries of the three optimization variables, the loss coefficients of the considered magnetic materials, the converter topology, the number of parallel converters and the frequency and inductance values of interest. In order to show the versatility of the algorithm, a wide variation of design parameters is considered, as presented in Table III. As can be seen, four converter configurations are obtained, for there are two topologies (2L and 3L) and they can have one buck-boost or two in parallel ($N_B = 1$ and $N_B = 2$).

TABLE III. DESIGN PARAMETERS OF THE ALGORITHM

Source	Parameters	
	Description	*Value*
Designer	Function to be minimized	Equivalent volume, V_e
	Converter topologies	2L, 3L
	Parallel converters, N_B	1, 2
	Boundaries of a	$[0,40]\ mm$
	Boundaries of R	$[0,6]\ mm$
	Boundaries of μ_r	$[26,90]$
	Boundaries of c_1	$[0.6,1.6]$
	Boundaries of c_2	$[0.8,2.0]$
	Max. winding factor, WF	40%
	Initial inductance range, L_0	$[40,1120]\ \mu H$
	Switching freq. range, f_{sw}	$[20,72]\ kHz$
	Magnetic materials	Sendust
Source	Sendust core characteristics	
	Description	*Value*
Datasheet	Core loss coeff., C_m	$-3.11 \cdot 10^{13}\mu_r^{-10.48} + 0.12$
	Core loss coeff., x	$2.673 \cdot 10^6 \mu_r^{-6.324} + 1.193$
	Core loss coeff., y	$-3.311 \cdot 10^6 \mu_r^{-5.16} + 2.19$
	H_{max} coefficient, p	$3.318 \cdot 10^5$
	H_{max} coefficient, q	-0.921

The results of the optimization tool for volume minimization are presented in Fig. 6 and Fig. 7 as color maps. In the top part of the figures, (a) and (b), the equivalent volume is depicted, while in the bottom part, (c) and (d), the power losses are represented. The depicted values are total values, e.g. for a two-level design with $N_B = 2$ and $L_0 = 100\ \mu H$, there are two 100-μH inductors in each parallel converter and the plotted volume comprise of the sum of the individual

equivalent volume of both inductors. The same applies to the total power losses. This way, the inductor designs can be directly compared, regardless the topology and number of parallel converters. Fig. 6 shows the designs for the 2L converter, regarding one, $N_B = 1$, and two parallel converters, $N_B = 2$. Fig. 7 presents the results for the 3L converter, with $N_B = 1$ and $N_B = 2$. The grey shaded areas of the color maps represent non-feasible designs.
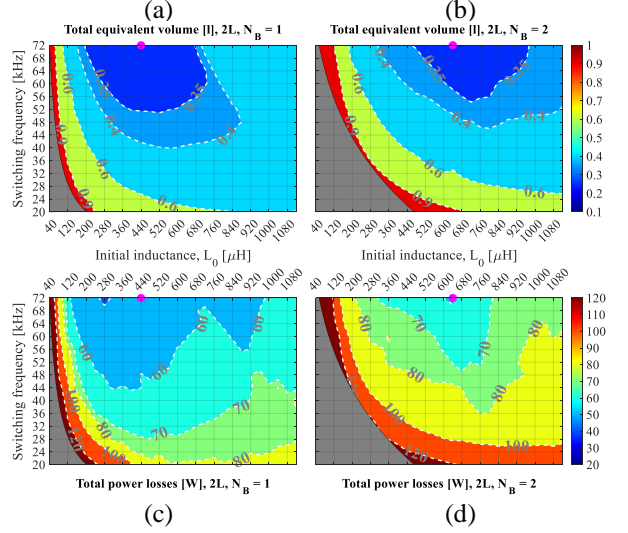

Fig. 6. Design results of the proposed algorithm for inductors implemented in a 2L buck-boost: (a) total eq. volume, $N_B = 1$, (b) total eq. volume, $N_B = 2$, (c) total power losses, $N_B = 1$, (d) total power losses, $N_B = 2$.
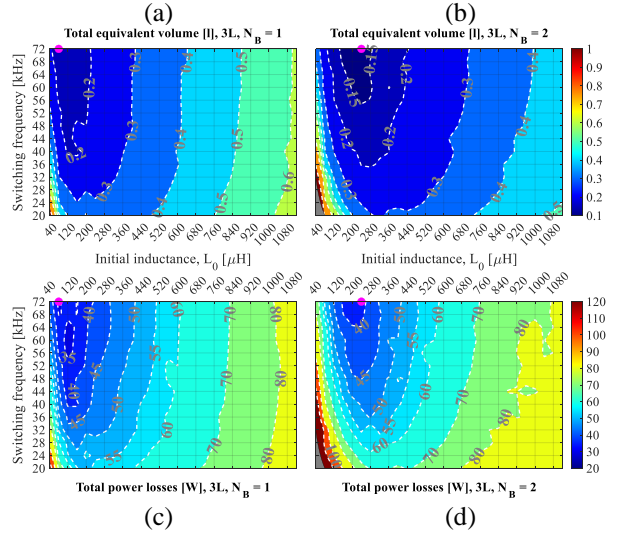

Fig. 7. Design results of the proposed algorithm for inductors implemented in a 3L buck-boost: (a) total eq. volume, $N_B = 1$, (b) total eq. volume, $N_B = 2$, (c) total power losses, $N_B = 1$, (d) total power losses, $N_B = 2$.

The optimal design for each configuration is pointed out in Fig. 6 and Fig. 7 with a round, magenta marker. The resultant number of inductors, total equivalent volume and total power losses are shown in Table IV. Attending to the results in Fig. 6 and Fig. 7, two key conclusions can be deduced: first, that the relationship between volume and inductance is not monotonic, thus the optimal design is not obtained at minimum inductance, due to the HF effects; second, in inductors implemented in a 3L buck-boost, the DC winding loss starts to be dominant at lower inductance values

than in the 2L case due to the three-level voltage, which means smaller current ripple and peak induction value for same operating conditions, thus lower core and AC winding losses. As a consequence, the optimal design in the 3L topology is obtained for smaller initial inductance values than in the 2L converter. Moreover, the total volume occupied by the optimal solution of the inductors in the 3L buck-boost can be half the volume of the optimal design in the 2L buck-boost, as shown in Table IV.

TABLE IV.   OPTIMAL DESIGN RESULTS OF THE INDUCTORS

Results	Converter configurations			
	2L, $N_B = 1$	2L, $N_B = 2$	3L, $N_B = 1$	3L, $N_B = 2$
L_0	440 μH	640 μH	80 μH	240 μH
f_{sw}	72 kHz	72 kHz	72 kHz	72 kHz
Nº of inductors	1, 440 μH	2, 640 μH each	2, 40 μH each	4, 120 μH each
Total V_e	0.29 l	0.28 l	0.15 l	0.13 l
Total P_{ind}	52.0 W	59.1 W	33.6 W	38.8 W

In order to take a deeper look into the results provided by the optimization algorithm, the power losses and equivalent volume for two selected switching frequencies (28 and 56 kHz) are presented in Fig. 8. The DC winding loss, AC winding loss and core loss are explicitly shown too. The influence of the switching frequency and the inductance value on the power losses can be easily analyzed from the results in Fig. 8 (a) – (d) for each of the four converter configurations. A few, small discontinuities in the evolution of V_e and P_{ind} with L_0 can be found in Fig. 8, because the coefficients c_1 and c_2 are discretely varied in the algorithm. As can be seen attending on the share of the three different loss components, regardless of the configuration, the greater the inductance value, the lower the HF losses (AC winding loss and core loss) and the higher the DC winding loss. For low inductance values, the HF effects are dominant, and volume and power losses are not minimum. Certain designs for low L_0 are not feasible and, thus, not plotted in Fig. 8. As previously mentioned, the optimal design is not obtained for minimum

inductance value in any of the configurations due to the HF effects, which makes it clear that they cannot be neglected in the design of inductors in switching converters. Actually, with 2L converter topology and $N_B = 2$ (see Fig. 8 (b)), the optimal design is obtained for $L_0 = 1080\ \mu H$ at 28 kHz and $L_0 = 720\ \mu H$ at 56 kHz, with the HF losses representing more than 50% of the total losses in both cases.

Parallelization of the inductors have a positive effect on the DC winding loss (the DC current intensity is shared by N_B inductors) and on the dissipation capacity, for there is a larger equivalent surface exposed to the air. However, parallelization has no effect on reducing the HF losses. As a consequence, if HF effects are dominant, changing from one inductor to two parallel inductors can be counterproductive, since AC power losses stay constant in each inductor, but now there are two of them instead of one. As a result, total V_e and P_{ind} can be greater with $N_B = 2$ than with $N_B = 1$. This is the case of designs in 2L buck-boost, especially at low f_{sw}, where HF effects have a great impact on the total power losses. In the 3L buck-boost, parallelization does lead to more compact solutions, except for low inductance values (typically, $L_0 < 160\ \mu H$), where HF effects are substantial. Finally, it has to be noted that the designs must fulfil not only the thermal constraint, but the core window and the saturation constraints too and that these constraints influence the design.

V.   DESIGN EXAMPLE

The proposed algorithm for designing inductors can be implemented into a more complex design tool, including the semiconductor system. This way, it is ensured that the inductor design is also feasible from the switches point of view. For instance, as mentioned in *Section IV*, the optimal inductor design is obtained at high switching frequency (72 kHz), which may not be reachable for the switches without overheating. Thus, considering both the filter and the semiconductor systems in the algorithm, allows to obtain a global optimal design of the converter.
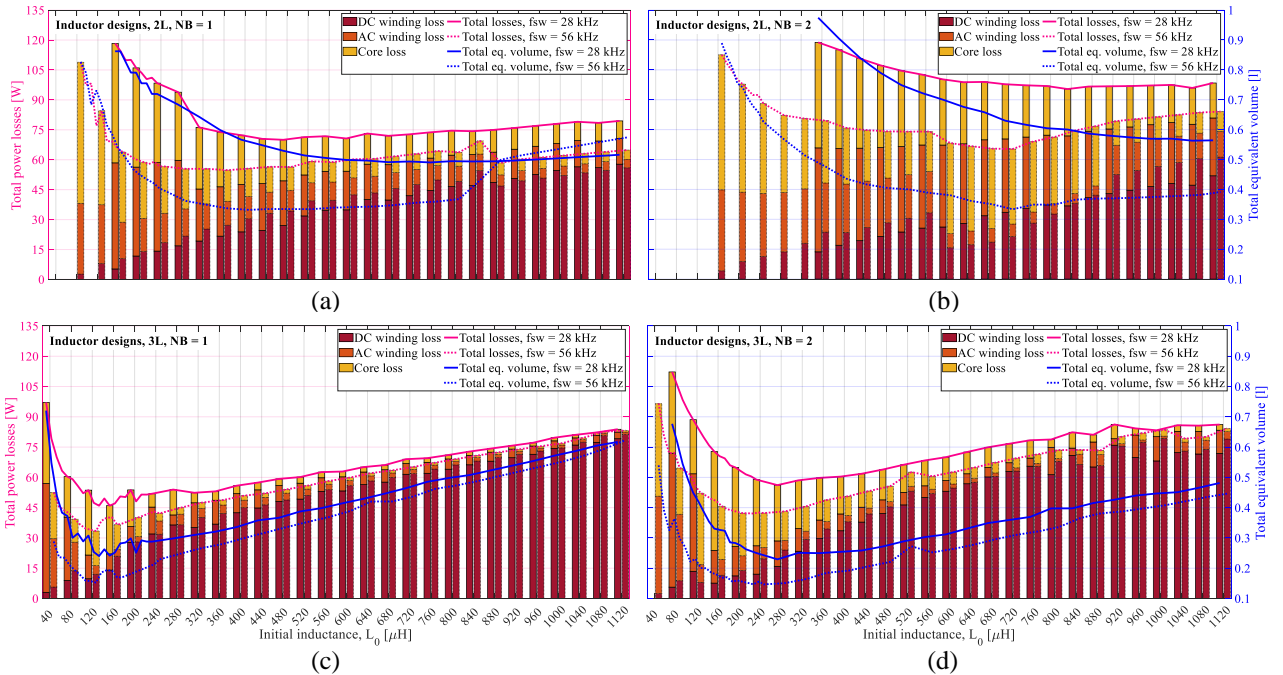

Fig. 8.   Total losses at 28 kHz and 56 kHz for inductors implemented in: (a) 2L buck-boost, $N_B = 1$, (b) 2L buck-boost, $N_B = 2$, (c) 3L buck-boost, $N_B = 1$, (d) 3L buck-boost, $N_B = 2$.

In this paper, a design example is provided regarding a 15-kW three-level buck-boost converter without parallelization. The SiC MOSFET module FF23MR12W1M1_B11 of Infineon is considered. The inductor design algorithm is run with the same parameters as in Table III, but only for a 3L topology and $N_B = 1$. For the switches, conduction and switching losses are calculated from the information available in the datasheet [22]. The semiconductors are thermally constrained as shown in the following expression:

$$(P_{con} + P_{sw})R_{th,j-s} \leq T_{j,des} - T_{s,des} \qquad (23)$$

where P_{con} and P_{sw} are the conduction and switching losses of the switch, respectively, $R_{th,j-s}$ is the junction-to-heatsink thermal resistance, $T_{j,des}$ is the design maximum allowable junction temperature and $T_{s,des}$ is the maximum allowable temperature of the heatsink. The datasheet of the FF23MR12W1M1_B11 module indicates that $T_{j,max} = 150\ ^\circ C$ under switching conditions. A safe margin of $25\ ^\circ C$ for the junction temperature and a maximum thermal rise of $35\ ^\circ C$ between the heatsink and the junction are defined. Hence, in this design example, $T_{j,des} = 125\ ^\circ C$ and $T_{s,des} = 90\ ^\circ C$ are selected. The thermal resistance is $R_{th,j-s} = 0.8\ ^\circ C/W$, as obtained from the module datasheet. For calculating the conduction losses, the SiC MOSFET operates whether in the first quadrant or the third quadrant. The share in the power losses of the body diode conduction, which only takes place during the dead time, is considered negligible.

The resultant designs are presented in Fig. 9, where (a) and (b) show the volume and power losses, respectively, of the two inductors of the output filter in the 3L, $N_B = 1$ buck-boost, (c) shows the total power losses (conduction and switching losses) of the switches, and (d) depicts the combined losses of inductors and switches. The areas shaded in red are non-feasible designs for the switches, that is, where the MOSFET SiC module cannot fulfil the thermal constraint in (23). As can be seen, the optimal design of the inductors alone (grey marker at $f_{sw} = 72\ kHz, L_0 = 80\ \mu H$ in Fig. 9) is not feasible anymore when considering the semiconductor system. This example shows the convenience of the holistic approach of the proposed algorithm, since it avoids designs based on local optimal and considers the interrelationship between the switches and the output inductors. For instance, a higher switching frequency can be positive for the inductors, but it leads to higher switching losses in the semiconductors.

The minimum volume design is marked in Fig. 9 with a round, magenta marker. The total equivalent volume is 0.16 l, which means that each inductor is 0.08 l. The total power losses (inductors + switches) are 175 W. As an alternative, the minimum losses design can be selected, which is shown in Fig. 9 with a triangular, magenta marker. As can be seen, the inductors are bulkier (0.24 l), but the total power losses are lower: 160 W. The designer can choose any of these two designs, depending on the preferred criterion. In this design example, achieving total minimum losses is prioritized. As a result, the $f_{sw} = 28\ kHz, L_0 = 160\ \mu H$ design is selected. The details of the designed inductors are presented in Table V.

As can be seen in the column *Algorithm* in Table V, the proposed inductor design methodology, since it has an analytical nature, provides a theoretical optimal design which is not commercial: the wire diameter is not standard, the number of turns is non-integer and the core dimensions do not

correspond to a commercial core. As a consequence, the design must be adapted to the closest practical design which fulfils the design constraints. This can be easily done by selecting appropriate core and wire gauge and by rounding the number of turns. In order to select an appropriate commercial core, both the geometry (a, c_1, c_2) and the permeability (μ_r) have to be contemplated.
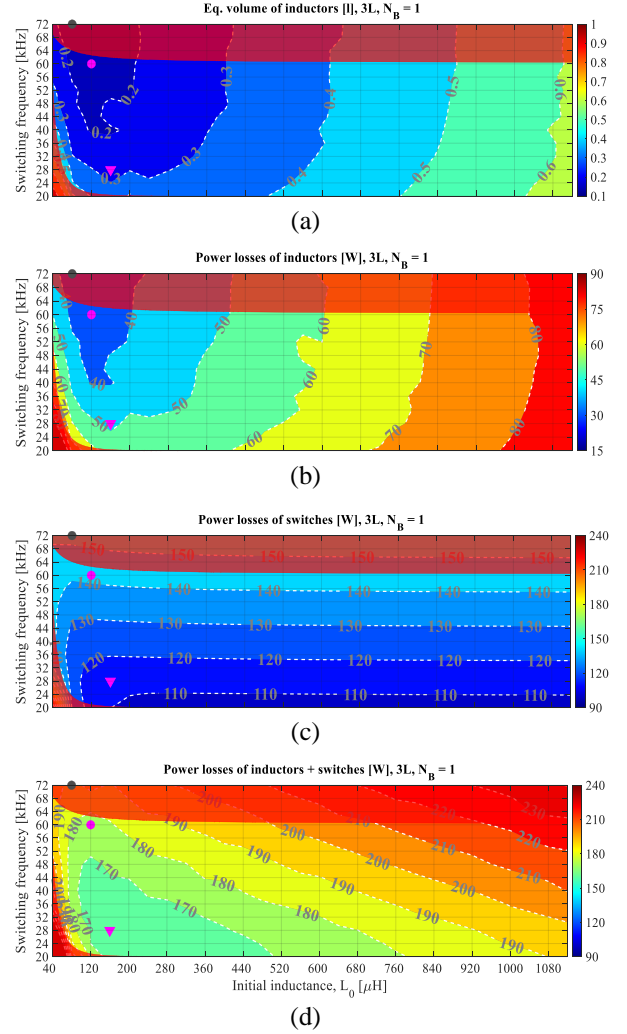

(a)

(b)

(c)

(d)

Fig. 9. Results of the proposed algorithm in a 3L buck-boost converter with $N_B = 1$, including feasibility of SiC MOSFET FF23MR12W1M1_B11: (a) total eq. volume of the inductors, (b) total power losses of the inductors, (c) power losses of the switches, (d) total power losses of inductors and switches.

In this design, commercial cores with $\mu_r = 60$ are to be considered and two shapes are selected due to their similarities to the theoretical design: OD467 and OD571 [21]. It is worth noting that, as obtained in this design, it can be necessary to stack two commercial cores in order to meet the height of the theoretical core. Regarding the wire, since the theoretical wire radius is 1.60 mm, the closest wire gauges are considered below (AWG9) and above (AWG8) that radius. In this design example, Commercial 1 (two stacked OD467 and AWG8) and Commercial 2 (two stacked OD571 and AWG8) designs are the most similar to the theoretical optimal design and are presented in Table V too. It is worth mentioning that the inductors are designed for a three-level converter with $N_B = 1$, thus the resultant optimal design is a total initial inductance $L_0 = 160\ \mu H$ split into two equal inductors of $80\ \mu H$. For this reason, in Table V, equivalent volume, core

loss and winding loss are presented for a single $80\text{-}\mu H$ inductor but pointing out that there will be two inductors. Attending to the two commercial designs, both have similar losses, while Commercial 1 is a more compact solution. Thus, Commercial 1 is the selected design.

TABLE V. OPTIMAL AND COMMERCIAL DESIGNS OF INDUCTORS IN A 15-kW, THREE-LEVEL BUCK-BOOST CONVERTER

Results	Designs		
	Algorithm	*Commercial 1*	*Commercial 2*
N° of inductors	2	2	2
$a\ [mm]$	16.24	12.15	16.2
$R\ [mm]$	1.60	1.63	1.63
μ_r	60	60	60
Core	-	OD467 (x2 stacked)	OD571 (x2 stacked)
Wire	-	AWG8	AWG8
c_1	0.68	0.96	0.79
c_2	1.84	3.11	1.99
N	16.23	16	16
$V_e\ [l]$	0.12 (x2)	0.12 (x2)	0.15 (x2)
$P_c\ [W]$	11.9 (x2)	12.1 (x2)	11.8 (x2)
$P_\omega\ [W]$	11.1 (x2)	11.6 (x2)	11.6 (x2)

VI. CONCLUSIONS

In this paper, an optimization algorithm is proposed for the design of toroidal powder inductors in DC-DC buck-boost converters. A complete parameterization of the inductor is introduced, allowing to express all dimensional characteristics, power losses and design constraints by means of three design variables. The high-frequency effects are included through appropriate core loss and winding loss models. The usefulness of the design algorithm is demonstrated by applying it to the design of toroidal inductors in a 15-kW EV charger, considering two different converter topologies. The results provided by the design tool allows the designer to easily identify the optimal design and analyze the effect of varying input parameters, such as number of parallel inductors, switching frequency and inductance value. Moreover, thanks to considering the high-frequency effects in the inductor, design misconceptions, such as aiming to the minimum inductance value for minimum volume, can be avoided. Finally, a design example comprising of a SiC MOSFET three-level converter is presented, showing how the inductor design algorithm can be combined with the semiconductor system design. An easy method to adapt the analytical, optimal design of the inductor to a commercial solution is introduced too.

REFERENCES

[1] E. Serban, M. Ordonez, C. Pondiche and D. Hulea, "Voltage and Power Balancing in Solar and Energy Storage Converters," *2019 IEEE Energy Conversion Congress and Exposition (ECCE)*, 2019, pp. 5832-5839, doi: 10.1109/ECCE.2019.8912301.

[2] M. Afkar, R. Gavagsaz-Ghoachani, M. Phattanasak, J. -P. Martin and S. Pierfederici, "Proposed System Based on a Three-Level Boost Converter to Mitigate Voltage Imbalance in Photovoltaic Power Generation Systems," in *IEEE Transactions on Power Electronics*, vol. 37, no. 2, pp. 2264-2282, Feb. 2022, doi: 10.1109/TPEL.2021.3105571.

[3] M. G. Molina, "Energy Storage and Power Electronics Technologies: A Strong Combination to Empower the Transformation to the Smart Grid," in *Proceedings of the IEEE*, vol. 105, no. 11, pp. 2191-2219, Nov. 2017, doi: 10.1109/JPROC.2017.2702627.

[4] A. Khalid, A. Stevenson and A. I. Sarwat, "Overview of Technical Specifications for Grid-Connected Microgrid Battery Energy Storage Systems," in *IEEE Access*, vol. 9, pp. 163554-163593, 2021, doi: 10.1109/ACCESS.2021.3132223.

[5] J. -Y. Kim, B. -S. Lee, Y. -J. Lee and J. -K. Kim, "Integrated Multi Mode Converter With Single Inductor for Fuel Cell Electric Vehicles," in *IEEE Transactions on Industrial Electronics*, vol. 69, no. 11, pp. 11001-11011, Nov. 2022, doi: 10.1109/TIE.2021.3118390.

[6] S. Dusmez, A. Hasanzadeh and A. Khaligh, "Comparative Analysis of Bidirectional Three-Level DC–DC Converter for Automotive Applications," in *IEEE Transactions on Industrial Electronics*, vol. 62, no. 5, pp. 3305-3315, May 2015, doi: 10.1109/TIE.2014.2336605.

[7] J. -Y. Kim, B. -S. Lee, D. -H. Kwon, D. -W. Lee and J. -K. Kim, "Low Voltage Charging Technique for Electric Vehicles With 800 V Battery," in *IEEE Transactions on Industrial Electronics*, vol. 69, no. 8, pp. 7890-7896, Aug. 2022, doi: 10.1109/TIE.2021.3109526.

[8] J. Imaoka, K. Okamoto, M. Shoyama, Y. Ishikura, M. Noah and M. Yamamoto, "Modeling, Magnetic Design, Simulation Methods, and Experimental Evaluation of Various Powder Cores Used in Power Converters Considering Their DC Superimposition Characteristics," in *IEEE Transactions on Power Electronics*, vol. 34, no. 9, pp. 9033-9051, Sept. 2019, doi: 10.1109/TPEL.2018.2886044.

[9] Dowell, P. L. "Effects of eddy currents in transformer windings." *Proceedings of the Institution of electrical Engineers*. Vol. 113. No. 8. IET Digital Library, 1966.

[10] C. Du, W. G. Hurley and D. Xu, "Design Methodology of Resonant Inductor in a ZVS Inverter," in *IEEE Journal of Emerging and Selected Topics in Power Electronics*, vol. 3, no. 4, pp. 1142-1150, Dec. 2015, doi: 10.1109/JESTPE.2015.2460996.

[11] F. Forest, E. LabourÉ, T. A. Meynard and V. Smet, "Design and Comparison of Inductors and Intercell Transformers for Filtering of PWM Inverter Output," in *IEEE Transactions on Power Electronics*, vol. 24, no. 3, pp. 812-821, March 2009, doi: 10.1109/TPEL.2008.2007900.

[12] T. Friedli, J. W. Kolar, J. Rodriguez and P. W. Wheeler, "Comparative Evaluation of Three-Phase AC–AC Matrix Converter and Voltage DC-Link Back-to-Back Converter Systems," in *IEEE Transactions on Industrial Electronics*, vol. 59, no. 12, pp. 4487-4510, Dec. 2012, doi: 10.1109/TIE.2011.2179278.

[13] R. P. Wojda and M. K. Kazimierczuk, "Winding Resistance and Power Loss of Inductors With Litz and Solid-Round Wires," in *IEEE Transactions on Industry Applications*, vol. 54, no. 4, pp. 3548-3557, July-Aug. 2018, doi: 10.1109/TIA.2018.2821647.

[14] A. Koran, S. Albatran and D. Alshorman, "Adaptive Switching Frequency Selection Based on Two-Step Efficiency Optimization for Grid-Connected Inverters," in *IEEE Access*, vol. 9, pp. 151741-151752, 2021, doi: 10.1109/ACCESS.2021.3126378.

[15] D. Elizondo, E. L. Barrios, P. Sanchis and A. Ursua, "Analytical Modeling of High-Frequency Winding Loss in Round-Wire Toroidal Inductors," *2020 IEEE 21st Workshop on Control and Modeling for Power Electronics (COMPEL)*, 2020, pp. 1-6, doi: 10.1109/COMPEL49091.2020.9265782.

[16] J. A. Ferreira, "Improved analytical modeling of conductive losses in magnetic components," in *IEEE Transactions on Power Electronics*, vol. 9, no. 1, pp. 127-131, Jan. 1994, doi: 10.1109/63.285503.

[17] S. A. Mulder, "Fit formulae for power loss in ferrites and their use in transformer design," in *Proc. PCIM*, 1993, pp. 345–359.

[18] E. L. Barrios, A. Ursúa, L. Marroyo and P. Sanchis, "Analytical Design Methodology for Litz-Wired High-Frequency Power Transformers," in *IEEE Transactions on Industrial Electronics*, vol. 62, no. 4, pp. 2103-2113, April 2015, doi: 10.1109/TIE.2014.2351786.

[19] I. Villar, U. Viscarret, I. Etxeberria-Otadui and A. Rufer, "Global Loss Evaluation Methods for Nonsinusoidally Fed Medium-Frequency Power Transformers," in *IEEE Transactions on Industrial Electronics*, vol. 56, no. 10, pp. 4132-4140, Oct. 2009, doi: 10.1109/TIE.2009.2021174.

[20] Magnetics, "Powder Cores," 2017. [Online]. Available: www.mag-inc.com.

[21] Changsung Corporation (CSC), "Magnetic Powder Cores, " ver. 15. [Online]. Available: www.changsung.com.

[22] Infineon, "FF23MR12W1M1_B11 Datasheet," V 2.2. [Online]. Available: www.infineon.com.